

SPIN-ORBIT-TORQUE-DRIVEN SWITCHING IN  
PERPENDICULAR-MAGNETIC-ANISOTROPY-BASED  
DEVICES FOR THE NON-VOLATILE MEMORY AND  
NEUROMORPHIC SYNAPSE APPLICATIONS

RAM SINGH YADAV



DEPARTMENT OF PHYSICS  
INDIAN INSTITUTE OF TECHNOLOGY DELHI  
APRIL 2025

© **Indian Institute of Technology Delhi (IITD), New Delhi, 2025**

**Spin-orbit-torque-driven switching in perpendicular-magnetic  
-anisotropy-based devices for non-volatile memory and neuromorphic  
synapse applications**

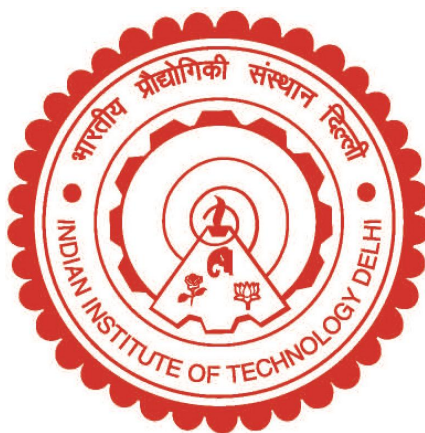
by

**Ram Singh Yadav**

Department of Physics

Submitted

in fulfillment of the requirements for the degree of Doctor of Philosophy  
to the



**INDIAN INSTITUTE OF TECHNOLOGY DELHI**

**April 2025**

## Certificate

This is to certify that the thesis entitled, **Spin-orbit-torque-driven switching in perpendicular-magnetic-anisotropy-based devices for non-volatile memory and neuromorphic synapse applications**, is being submitted by **Mr. Ram Singh Yadav** to the Department of Physics, Indian Institute of Technology Delhi, for the award of the degree of **Doctor of Philosophy**. This work is a record of bonafide research conducted by him. He has worked under my supervision and guidance and has fulfilled all the requirements for the submission of this thesis. In my opinion, the work has reached the requisite standard.

The results presented in this thesis have not been submitted, either in part or in full, to any other University or Institute for the award of any degree or diploma.

*Debanjan Bhowmik*

---

**Prof. Prof. P. K. Muduli**

Professor

Department of Physics

Indian Institute of Technology Delhi

New Delhi - 110016

India.

Date:

**Prof. Debanjan Bhowmik**

Associate Professor

Department of Electrical Engineering

Indian Institute of Technology Bombay

Maharashtra - 400076,

India.

Date:

## Acknowledgements

I would like to express my heartfelt gratitude to everyone who made my Ph.D. journey more enjoyable through their deliberate support, guidance, and encouragement, helping me complete this unforgettable endeavor.

First and foremost, I extend my deepest appreciation to my supervisors, Prof. P. K. Muduli and Prof. Debanjan Bhowmik, for their unwavering support, encouragement, and invaluable guidance throughout this research. I am thankful to both supervisors for giving me the opportunity to work on fascinating research topics and for continuously monitoring and providing guidance throughout my Ph.D. journey. I am grateful for their time and efforts in engaging in scientific discussions despite their busy schedules. I would like to give special thanks to Prof. D. Bhowmik for his support during the SOT switching optimization and for teaching me the basics of PMA and SOT switching through our long online discussions. Without Prof. Bhowmik, we could not have envisioned neuromorphic computing using experimentally observed data, which was made possible only because of him. I am also sincerely thankful to the Student Research Committee (SRC) members, Prof. Pankaj Srivastava, Prof. Sujit Manna, and Prof. Rahul Mishra, for their insightful scientific advice, thoughtful comments, and valuable suggestions during my SRC presentations.

I am deeply grateful to the Department of Physics for providing the necessary departmental facilities and to the Central Research Facility (CRF) and the Nanoscale Research Facility (NRF) for offering device fabrication resources. I also appreciate the availability of high-performance computing (HPC) for computational needs. My heartfelt thanks go to the Ministry of Human Resource Development, Government of India, for their financial support throughout my research.

I am immensely thankful to my senior labmates for fostering a welcoming and supportive atmosphere from the very beginning of my research journey. Special thanks go to Dr. Akash Kumar for his unwavering assistance and encouragement during my initial days in the lab and his guidance in operating the instruments. I am also grateful to Dr. Naveen Sisodia for teaching me LabVIEW, which has been instrumental for instrument automation. My sincere gratitude extends to Dr. Raghav Sharma for his continuous support during the optimization of the SOT switching setup and for generously sharing his knowledge during his visits to IIT Delhi. I deeply appreciate Dr. Niru Chaudhary for engaging in scientific discussions and Dr. Kacho Imtiyaz Ali Khan for sharing his expertise on Mumax3 and XRD. A special thanks to Ms. Pankhuri Gupta for her discussions, knowledge sharing on device fabrication, and steadfast support throughout my Ph.D. journey.

I am truly grateful to my lab batchmates, Dr. Rekha Agrawal and Dr. Himanshu, for their helpful discussions and continuous assistance, especially during the challenging period of my dengue illness. My thanks also go to Dr. Richa Mudgal for her support with mask fabrication and for reviewing the experimental section. I extend my appreciation to Ms. Nidhi Kandwal for proof reading my thesis and engaging in thoughtful discussions, as well as to Ms. Vaishali Yadav for her help with device fabrication.

I also acknowledge my juniors: Neha Garg, Aman Saxena, Deeksha Gupta, Azminul Jaman, Upasna Bordoloi, Namrata Bansal, Ujjawal Rathore, Uzer Ahmad, Alen John, Jasmeen Virk, Deeksha Khandelwal, Ankit Chauhan, Mahatva Jain, Dev Goyal, and Aryaman Gogoi for their contributions and meaningful discussions. A special thanks to my friends: Amar Kumar, Vinit Kumar, Pankaj, and Saurabh—for their constant support during my Ph.D. journey. I would also like to express my gratitude to Mr. S.P. Neelam for his inspiration and motivation during every meeting.

Finally, I extend my heartfelt thanks to my parents and family. This Ph.D. journey would not have been possible without their unwavering support and encouragement. I am particularly grateful to my elder sister for her unconditional support in everything.

*I dedicate this thesis to my parents.*

Ram Singh Yadav

## Abstract

This dissertation investigates the development and characterization of novel spintronic devices for neuromorphic computing applications. We focus on optimizing spin-orbit torque (SOT) switching and demonstrating synaptic behavior in various material systems. We explore the synaptic behavior in two types of perpendicularly magnetized materials and field-free SOT switching using a quantum material.

In the thesis, first, we optimized the PMA in (Pt/Co/SiO<sub>2</sub>) and demonstrated spin-orbit torque (SOT) switching. Following this, we revealed the presence of multiple *mixed states* in Pt/Co/SiO<sub>2</sub>. These *mixed states* correspond to intermediate magnetization configurations between two saturated states: all magnetic moments aligned vertically up and all moments aligned vertically down (with the ferromagnetic layer exhibiting PMA). These *mixed states* are modulated through in-plane current pulses, inducing SOT at the heavy-metal-ferromagnet interface. This allowed us to demonstrate long-term potentiation (LTP) and long-term depression (LTD) in the device, mimicking synaptic behavior. Experimentally, the synaptic bit resolution was determined to be 5 (approximately 30 distinguishable states) by measuring the stability of the *mixed states*. Additionally, the non-linearity and asymmetry in the obtained LTP and LTD are quantified experimentally and qualitatively explained through micromagnetic modeling. Micromagnetic Modelling is carried out for two scenarios: one without defects and another with edge defects. In the absence of defects, domain-wall motion causes non-linearity in the synaptic behavior, whereas edge defects restrict domain-wall motion, resulting in linear and symmetric synaptic behavior. Achieving high linearity and symmetry in the synaptic weight-update characteristic is critical for attaining high classification or regression accuracy in on-chip learning simulations.

Subsequently, we explored new heterostructures with high thermal stability and comparable switching current densities. SOT switching is experimentally demonstrated in a heavy-metal (Pt)/ferromagnetic metal (Co) gradient multilayer device, where the thickness of each Co layer remained fixed at 0.5 nm, while the Pt layer thickness increased from bottom to top (1 nm to 3 nm in increments of 0.4 nm). Using the thermally assisted SOT switching model on pulse-duration-dependent switching measurements, the thermal stability factor was determined to be 65 (across multiple devices), significantly higher than that of single-Pt-Co-layer-based devices (30). Notably, the switching current density remained similar for both types of devices. Additionally, the synaptic behavior of the gradient multilayer device was experimentally demonstrated, with 30 stable and distinguishable states controlled through positive current pulses (LTP) and 24 such states through negative pulses (LTD). Using non-ideality coefficients extracted from the experimentally obtained

LTP and LTD plots, the on-chip inference and learning performance of neuromorphic crossbar arrays composed of such devices are simulated.

In the final part, we explored quantum materials possessing y- and z-spin polarization due to the SHE and MSHE, respectively. The z-spin polarization is particularly useful for achieving field-free switching. Nearly 100 % field-free switching is demonstrated at a current density of  $6.1 \times 10^6$  A/cm<sup>2</sup> with a pulse width of 200  $\mu$ s. These results pave the way for energy-efficient SOT-MRAM and zero-field synapse devices for future neuromorphic computing systems.

Overall, the thesis advances the understanding and development of energy-efficient spintronic devices for neuromorphic computing.

## सारांश

यह शोध प्रबंध न्यूरोमॉर्फिक कंप्यूटिंग अनुप्रयोगों के लिए नवीन स्पिंट्रॉनिक यंत्र के विकास और विशेषताओं की जाँच करता है। हम स्पिन-ऑर्बिट टॉर्क (एसओटी) स्विचिंग को बेहतर बनाने और विभिन्न पदार्थ के सिस्टम्स में सिनेट्रिक बिहेवियर प्रदर्शित करने पर ध्यान केंद्रित करते हैं। हम दो प्रकार की परपेंडिक्युलरली मैग्नेटाइज्ड पदार्थ और एक क्वांटम पदार्थ का उपयोग करते हुए फील्ड-फ्री एसओटी स्विचिंग में सिनेट्रिक व्यवहार का अध्ययन करते हैं।

शोध प्रबंध के पहले भाग में, हमने  $(Pt/Co/SiO_2)$  में पीएमए को ऑप्टिमाइज़ किया और एसओटी स्विचिंग प्रदर्शित की। इसके बाद, हमने  $Pt/Co/SiO_2$  में कई मिश्रित अवस्था की उपस्थिति दर्शाई, जो दो सैचुरेटेड अवस्था (सभी मैग्नेटिक मोमेंट्स ऊर्ध्व दिशा में ऊपर और सभी नीचे) के बीच इंटरमीडिएट मैग्नेटाइजेशन कॉन्फ़िगरेशन्स को दर्शाती हैं। ये मिक्स्ड अवस्था, इन-प्लेन करंट पल्सेस द्वारा मॉड्युलेट की जाती हैं, जो हेवी-मेटल-फेरोमैग्नेट इंटरफेस पर एसओटी प्रेरित करती हैं। इससे हमें लॉन्ग-टर्म पोटेण्शिएशन (LTP) और लॉन्ग-टर्म डिप्रेसन (LTD) को प्रदर्शित करने में सफलता मिली, जो सिनेट्रिक व्यवहार का अनुकरण करते हैं। प्रयोगात्मक रूप से, मिश्रित अवस्था की स्थिरता को मापकर सिनेट्रिक बिट रिज़ॉल्यूशन 5 (लगभग 30 अलग-अलग अवस्थाएँ) निर्धारित किया गया। प्राप्त LTP और LTD में गैर-रैखिकता और असममिति को मापा गया और माइक्रोमैग्नेटिक मॉडलिंग द्वारा गुणात्मक रूप से समझाया गया। माइक्रोमैग्नेटिक मॉडलिंग दो परिदृश्यों के लिए की गई – एक बिना डिफेक्ट्स के और दूसरा एज डिफेक्ट्स के साथ। बिना डिफेक्ट्स की स्थिति में, डोमेन-वॉल मोशन सिनेट्रिक बिहेवियर में गैर-रैखिकता उत्पन्न करता है, जबकि एज डिफेक्ट्स, डोमेन-वॉल मोशन को सीमित करते हैं, जिससे सिनेट्रिक बिहेवियर अधिक रैखिक और सममित बनता है। सिनेट्रिक वेट-अपडेट कैरेक्टरिस्टिक में उच्च रैखिकता और सममिति प्राप्त करना, ऑन-चिप लर्निंग सिमुलेशन्स में उच्च क्लासिफिकेशन या रिग्रेसन एक्यूरेसी के लिए महत्वपूर्ण है।

इसके बाद, हमने नई हेटरोस्ट्रक्चर्स का अध्ययन किया जिनमें उच्च तापीय स्थिरता और तुलनीय स्विचिंग धारा घनत्व थीं। एसओटी स्विचिंग को एक हेवी-मेटल (Pt)/फेरोमैग्नेटिक मेटल (Co) ग्रेडिएंट बहुपरत यंत्र में प्रदर्शित किया गया, जहाँ प्रत्येक Co लेयर की मोटाई 0.5 nm निश्चित रखी गई, जबकि Pt परत की मोटाई नीचे से ऊपर की ओर क्रमशः 1 nm से 3 nm तक (0.4 nm के अंतराल में) बढ़ाई गई। थर्मली असिस्टेड एसओटी स्विचिंग मॉडल का उपयोग करते हुए, पल्स-इयूरेशन-डिपेंडेंट स्विचिंग मेज़रमेंट्स से थर्मल स्टेबिलिटी फैक्टर 65 (कई यंत्र में)

निर्धारित किया गया, जो कि एकल Pt-Co लेयर आधारित यंत्र (30) की तुलना में काफी अधिक था। विशेष रूप से, दोनों प्रकार के यंत्र के लिए स्विचिंग धारा घनत्व लगभग समान रही। इसके अतिरिक्त, ग्रेडिएंट मल्टीलेयर यंत्र में सिनेप्टिक व्यवहार को भी प्रदर्शित किया गया, जिसमें पॉजिटिव करंट पल्सेस (LTP) द्वारा 30 स्थिर व अलग-अलग अवस्थाएँ तथा नेगेटिव पल्सेस (LTD) द्वारा 24 अवस्थाएँ नियंत्रित की गईं। प्रयोगात्मक रूप से प्राप्त LTP और LTD प्लॉट्स से निकाले गए नॉन-आइडियलिटी कोएफिशिएंट्स का उपयोग करके, ऐसे यंत्र से बने न्यूरोमॉर्फिक क्रॉसबार एरेज के ऑन-चिप इन्फरेंस और लर्निंग परफॉर्मंस का अनुकरण किया गया

अंतिम भाग में, हमने ऐसे क्वांटम पदार्थ का अध्ययन किया जो SHE और MSHE के कारण  $y$ - और  $z$ -स्पिन पोलराइजेशन दर्शाते हैं।  $z$ -स्पिन पोलराइजेशन, विशेष रूप से फील्ड-फ्री स्विचिंग प्राप्त करने में उपयोगी है। लगभग 100% फील्ड-फ्री स्विचिंग को  $6.1 \times 10^6 A/cm^2$  की धारा घनत्व और  $200 \mu s$  की पल्स विड्थ पर प्रदर्शित किया गया। ये परिणाम भविष्य के न्यूरोमॉर्फिक कंप्यूटिंग सिस्टम्स के लिए ऊर्जा-कुशल एसओटी-एमआरएम और जीरो-फील्ड सिनेप्स यंत्र का मार्ग प्रशस्त करते हैं।

कुल मिलाकर, यह शोध-प्रबन्ध न्यूरोमॉर्फिक कंप्यूटिंग के लिए ऊर्जा-कुशल स्पिन्ट्रॉनिक यंत्र की समझ और विकास को आगे बढ़ाती है।

# Contents

<b>Certificate</b>	<b>i</b>
<b>Acknowledgements</b>	<b>iv</b>
<b>Abstract</b>	<b>vi</b>
<b>List of Figures</b>	<b>xv</b>
<b>List of Tables</b>	<b>xxvi</b>
<b>1 Introduction</b>	<b>1</b>
1.1 Spintronics-based non-volatile memory (NVM) . . . . .	1
1.2 Neuromorphic Computing . . . . .	3
1.3 Magnetic anisotropy . . . . .	6
1.3.1 Demagnetizing-field-based anisotropy . . . . .	6
1.3.2 Surface/Interface anisotropy . . . . .	6
1.4 Magnetic interactions . . . . .	7
1.4.1 Zeeman interaction . . . . .	8
1.4.2 Heisenberg exchange interaction . . . . .	8
1.4.3 Dzyaloshinskii-Moriya interaction (DMI) . . . . .	9

1.4.4	Domain Wall in thin film . . . . .	9
1.5	Magnetization Dynamics . . . . .	10
1.5.1	Spin Hall effect (SHE) . . . . .	11
1.5.2	Spin-orbit torques (SOTs) . . . . .	12
1.5.3	Tunneling magnetoresistance (TMR) . . . . .	13
1.6	SOT-Driven Domain-wall-device-based neuromorphic computing . . . . .	14
1.7	Organization of Thesis Chapters . . . . .	16
<b>2</b>	<b>Experimental and simulation details</b>	<b>19</b>
2.1	Thin film deposition: Magnetron sputtering . . . . .	19
2.2	Thin film characterization . . . . .	20
2.2.1	X-ray Diffraction (XRD) . . . . .	21
2.2.2	X-ray Reflectivity (XRR) . . . . .	22
2.2.3	Magnetic Property Measurement System-Superconducting Quantum Interference Device . . . . .	23
2.3	Fabrications of Hall bar devices using optical lithography . . . . .	24
2.4	Device characterization . . . . .	27
2.4.1	Anomalous Hall effect measurements (AHE) . . . . .	27
2.4.2	Spin-orbit torque efficiency quantification . . . . .	29
2.4.3	SOT Switching experiment . . . . .	35
2.5	Magneto-optic Kerr effect (MOKE) measurements . . . . .	38
2.6	MOKE imaging . . . . .	39
2.7	Simulation details . . . . .	40
2.7.1	Micromagnetic modeling using <i>Mumax</i> <sup>3</sup> . . . . .	40

<b>3</b>	<b>Spin-orbit torque switching and synaptic behavior in Pt/Co/SiO<sub>2</sub> heterostructures</b>	<b>43</b>
3.1	Introduction . . . . .	43
3.1.1	Our Contributions . . . . .	44
3.2	Experimental details . . . . .	46
3.3	Results and Discussion . . . . .	47
3.3.1	Thin film characterization . . . . .	47
3.3.2	Device characterization . . . . .	49
3.4	Conclusion . . . . .	58
<b>4</b>	<b>Micromagnetic Modeling of non- linear synaptic behavior for neuromorphic computing</b>	<b>59</b>
4.1	Introduction . . . . .	59
4.2	Micromagnetic simulation of the Domain-Wall Synapse Device in the Absence and Presence of Edge Defects . . . . .	62
4.2.1	Simulation Methodology and Parameter Values . . . . .	62
4.2.2	Simulation Results: Synaptic Characteristics . . . . .	65
4.2.3	Role of Thermal Field . . . . .	69
4.3	Discussions . . . . .	70
4.3.1	Device Fabrication Feasibility . . . . .	70
4.3.2	Novel Materials . . . . .	70
4.3.3	Scaling Issues . . . . .	71
4.4	Conclusion . . . . .	73
<b>5</b>	<b>Spin-orbit torque switching and synaptic behavior in gradient multilayer</b>	<b>75</b>
5.1	Introduction . . . . .	75

5.2	Experimental Details . . . . .	78
5.2.1	Sample preparation . . . . .	78
5.2.2	Structural and magnetic characterization . . . . .	79
5.2.3	Electrical characterization . . . . .	79
5.2.4	MOKE microscopy . . . . .	79
5.3	Results and Discussions . . . . .	80
5.3.1	Material Characterization: Perpendicular Magnetic Anisotropy (PMA) . . . . .	80
5.3.2	Device Characterization: Spin-Orbit Torque (SOT) Switching and Thermal Stability . . . . .	82
5.3.3	Device Characterization: Harmonic Hall measurements . . . . .	87
5.3.4	Device Characterization: SOT-Driven Synaptic Behaviour . . . . .	89
5.4	Discussions . . . . .	93
5.5	Conclusion . . . . .	95
<b>6</b>	<b>Field-free switching using Mn<sub>3</sub>Sn as a spin current source</b>	<b>97</b>
6.1	Introduction . . . . .	97
6.2	Experimental details . . . . .	99
6.2.1	Sample preparation . . . . .	99
6.2.2	Structural and magnetic characterization . . . . .	99
6.2.3	MOKE microscopy . . . . .	99
6.3	Results and Discussions . . . . .	100
6.3.1	Thin film characterization . . . . .	100
6.3.2	Device characterization . . . . .	102
6.4	Mechanism of field-free switching . . . . .	106

6.4.1 Conclusion . . . . .	107
<b>7 Summary and outlook</b>	<b>109</b>
7.1 Summary of Thesis . . . . .	109
7.2 Future Outlook . . . . .	111
<b>Bibliography</b>	<b>113</b>
<b>Publications</b>	<b>125</b>
<b>Biodata</b>	<b>129</b>

# List of Figures

1.1	Schematic of MRAM: (a) STT-MRAM (b) SOT-MRAM device configurations. The light blue, light gray, and purple colors are fixed, insulating, and free layers, respectively. The white arrow represents the magnetization direction, while the black one represents the current direction. . . . .	2
1.2	Schematic of the Von Neumann architecture, used in the conventional computer in which memory and computing unit are separated . . . . .	3
1.3	Neuromorphic/in-memory computing. . . . .	4
1.4	Schematic of a crossbar array that makes use of synapses and non-linear activation function circuits to implement a layer of a non-spiking neural network, or artificial neural network (ANN). Ideal conductance/ weight update characteristic of a synapse device needed for on-chip learning of an ANN: linearity for both conductance going up (long-term potentiation, or LTP) and down (long-term depression, or LTD), under the application of identical programming pulses, and symmetry between LTP and LTD. . . . .	5
1.5	In-plane to out-of-plane magnetic anisotropy transition with the thickness of the Co layer in the (Co/Pd) multilayer. Figure taken from [40] . . . . .	7
1.6	Schematic of (a) alignment of neighboring spins due to Heisenberg interaction, (b) Dzyaloshinskii-Moriya interaction, and (c) origin of DMI in HM/FM system. . . . .	8
1.7	Different types of the domain wall in PMA-based samples. . . . .	10
1.8	Magnetization dynamics under external magnetic field. . . . .	11
1.9	Schematic of spin current generation due to spin Hall effect. . . . .	12

1.10	Magnetization dynamics showing the directions of damping-like torque and field-like torque in the presence of spin current. . . . .	13
1.11	Schematic of the TMR: (a) Tunneling of up and down spin electrons from FM1 to FM2 via oxide layer (insulating layer) for parallel configuration, low resistance state (b) Up and down spin electrons tunneling for the antiparallel configuration, high resistance state . . . . .	14
1.12	SOT-driven domain wall motion in heavy metal/ferromagnet/oxide heterostructures: (a) DW at the center of the ferromagnetic layer (b) DW moves right due to SOT when the charge current is applied. . . . .	16
1.13	Schematic of magnetic tunnel junctions (MTJs): A thin insulating layer is sandwiched between the fixed and free layers, which works as a tunneling layer. TMR is utilized for the determination of the relative orientation of both layers. . . . .	16
2.1	Schematic diagram of thin film growth process using magnetron sputtering technique. (a) Sputtering chamber with the various components (b) In the deposition process of the magnetron sputtering, Ar ion bombarded on the target materials and sputtered out it. . . . .	20
2.2	(a) Schematic illustration of X-ray diffraction (XRD) measurements. (b) Schematic representation of X-ray diffraction from the crystal planes in a sample. . . . .	21
2.3	(a) Schematic of the XRR measurements; total external reflection takes place for ( $\theta < \theta_C$ ), (b) X-ray penetrate for incident angle ( $\theta > \theta_C$ ) and interference of reflected X-ray from different surface/interface will give Kiessig fringes. (c) The measured XRR spectra of Ta/TaO <sub>x</sub> thin film with fitted data; the black circle for measured data and red solid line for the fitted data. . . . .	22
2.4	Schematic and working principle of the SQUID . . . . .	23
2.5	Schematic illustrations of Hall bar fabrication process flow using optical lithography (a) first-level lithography process flow for the fabrication of Hall bar. (b) second-level lithography steps for the deposition of the contact pad, which is utilized for the transport measurements. . . . .	25

2.6	Schematic of Argon milling, high-energy Argon ion incident on the sample, and materials sputtered out. . . . .	26
2.7	AHE measurements setup: The measurements setup consists of a Keithely 6221 current source for applying current, a Keithely 2182A nanovoltmeter for measuring the transverse voltage, and an electromagnet to sweep the out-of-plane magnetic field. . . . .	28
2.8	(a) Schematics of anomalous Hall measurements: Current is applied in the $x$ -direction, and Hall voltage is measured in the $y$ -direction while sweeping the out-of-plane magnetic field ( $H_z$ ). (b) Anomalous Hall resistance ( $R_{xy}$ ) vs. out-of-plane magnetic field ( $H_z$ ) for gradient-Pt/Co multilayer samples. . . . .	29
2.9	Schematic diagram of harmonics Hall measurements configurations: (a) Longitudinal configuration: applied current and magnetic field are colinear to each other (b) Transverse configuration: applied current and magnetic field are perpendicular to each other. . . . .	30
2.10	Schematic diagram of the harmonic Hall measurement setup: The experimental setup includes two electromagnets, one generating an out-of-plane magnetic field ( $H_z$ ) and the other an in-plane magnetic field ( $H_x$ ). A low-frequency AC current is injected using a Keithley 6211 current source, and the first and second harmonic voltages are measured using an SR-860 lock-in amplifier. . . . .	31
2.11	(a) The first harmonic Hall and (b) the second harmonic Hall spectra of the gradient-Pt/Co multilayer system. . . . .	32
2.12	(a) Schematic diagram of hysteresis loop shift measurement setup: A constant DC in-plane magnetic field ( $H_x$ ) is applied during anomalous Hall measurement. DC current is applied using a Keithely 6221 current source, and Hall voltage is measured using a Keithely 2182A nanovoltmeter. (b) Schematic of hysteresis loop shift measurements (c) Hysteresis loop shifts under opposite current polarities: under 10 mA, hysteresis loop shifts towards positive $H_z$ , and under -10 mA, hysteresis loop shifts towards negative $H_z$ . . . . .	34

2.13	Current-induced magnetization switching mechanism (a) Unstable state with magnetization in $+z$ state, $H_{DL}$ and $H_x$ parallel (b) Stable state with magnetization in $-z$ state. $H_x$ is an in-plane external magnetic field that is collinear to the current direction, $\tau_{DL}$ and $H_{DL}$ are damping-like torque and effective field due to damping-like torque, respectively. . . . .	36
2.14	(a) Schematic diagram of SOT magnetization switching experimental setup. The experimental setup was equipped with a Keithely 6221 current source and a Keithely 2182A nanovoltmeter, both operated in pulsed delta mode. A quadruple magnet was utilized so in-plane and out-of-plane magnetic fields will be applied without any mechanical movement of the sample stage. (b) Schematic of SOT switching measurements, in-plane current pulses are applied in the $x$ -direction and anomalous Hall resistance measured in the $y$ -direction in the presence of in-plane magnetic ( $H_x$ ) (c) Current pulse sequence used for SOT switching, write current to manipulate the magnetization states and read current pulse to read the magnetization state. (d) SOT switching loop ( $R_{xy}$ vs. write current) of Pt/Co/SiO <sub>2</sub> for $H_x = \pm 3000$ G, switching polarity changed when the in-plane magnetic field was changed. . . . .	37
2.15	MOKE magnetometry (a) Longitudinal configuration (b) Polar configuration and (c) Transverse configuration . . . . .	39
2.16	(a) Magvision MOKE microscopy from Vertisis Technology (b) Schematic illustration of MOKE microscopy for Polar configuration. . . . .	39
3.1	XRR measured data with simulated data using recursive Parratt-formalism (a) Ta (b) Pt (c) Co and (d) SiO <sub>2</sub> . . . . .	47
3.2	(a) Material stack for the ferromagnetic thin film used (b) Out-of-plane magnetization $M_z$ (normalized through dividing by saturation magnetization $M_s$ ) vs. out-of-plane magnetic field ( $H_z$ ), as measured for the thin film through SQUID for different thicknesses of SiO <sub>2</sub> layer (c) In-plane magnetization $M_x$ (normalized through dividing by $M_s$ ) vs. in-plane magnetic field ( $H_x$ ), also measured through SQUID. (d) Anisotropy field $H_k$ and $K_{eff}$ vs the thickness of the SiO <sub>2</sub> layer. . .	48

3.3	(a) Optical-microscopy-based image of a Hall bar device fabricated from the thin-film stack of Fig. 3.2(a). Directions in which read current ( $I_x$ ) and write current are applied, Hall voltage ( $V_y$ ) is measured, and in-plane magnetic field ( $H_x$ ) is applied are shown. Ratio of $V_y$ to $I_x$ is the anomalous Hall resistance ( $R_{xy}$ ), proportional to out-of-plane magnetization $M_z$ . (b) $R_{xy}$ vs write current (applied in the form of pulses) when $H_x = 100, 250, 500, 1000, 2000$ and $3000$ G (c) $R_{xy}$ vs write current when $H_x = -100, -250, -500, -1000, -2000$ and $-3000$ G. Full switching between vertically up ( $M_z = 1$ ) and all down ( $M_z = -1$ ) happens when pulse magnitude $\geq 34$ mA ( $3.4 \times 10^7$ A/cm <sup>2</sup> ) approximately for $H_x = \pm 3000$ G . . . . .	50
3.4	Minor SOT switching loop: $R_{xy}$ vs write current pulse, the maximum write current pulses ranges from 40 mA to 60 mA. All the measurements were carried out using $100\mu s$ pulses for $H_x = -3000$ G at room temperature. Mixed states, with magnetization configuration in between vertically up and down states, are formed for lower values of current which are used for synaptic behaviour (LTP/ LTD) in Fig.) 3.6 and Fig. 3.7. . . . .	51
3.5	(a) Schematic of the hysteresis loop shift measurements (b) Hysteresis loop shift under opposite current polarities: under 10 mA, hysteresis loop shifts towards positive Hz, and under -10 mA, hysteresis loop shifts towards negative Hz (c) Effective perpendicular magnetic field $H_{eff}^z$ as a function of current under $H_x = \pm 3000$ G . . . . .	53
3.6	(a) In the presence of a constant -3000 G in-plane field ( $H_x$ ), the following sequence of write current pulses is applied to the device: 5 initialization pulses (-55 mA) are applied (pulse number $n = 1$ to 5), then 80 positive pulses of magnitude 20 mA, or $2 \times 10^7$ A/cm <sup>2</sup> ( $n = 6$ to 85) to cause synaptic potentiation/ LTP (increase of $R_{xy}$ ), and then 80 negative pulses of magnitude 20 mA ( $n = 86$ to 165) to cause depression/ LTD (decrease of $R_{xy}$ ). Some of the states are labelled based on the pulse numbers ( $n$ ) at which they are obtained. (b) $R_{xy}$ vs time for the states labeled in (a) shows their stability. Average fluctuation of $R_{xy}$ over time for each state is also mentioned next to the corresponding plot as $\sigma_{xy}$ . (c) Difference in $R_{xy}$ ( $\Delta R_{xy}$ ) between two consecutive states, numbered $n + 1$ and $n$ , is plotted as a function of $n$ . Since $\sigma_{xy}$ is in the order of $10^{-4}$ $\Omega$ in (b), any state with $\Delta R_{xy}$ one order higher than that (i.e, above the red dashed line) is considered as a synaptic state; any state below that line is discarded. . . . .	54

3.7 (a) Instead of applying a negative pulse, if we apply two negative pulses (-20 mA each) and a +20 mA pulse as a single negative pulse unit (labelled as ‘LTD pulse unit’ here), the downward jump after the first -20 mA pulse in Fig. 3.6(a) can be cancelled by an equal upward jump. After carrying out this adjustment on the experimental data for 30 positive and 30 negative pulses, we plot  $R_{xy}$  vs pulse number ( $n$ ) ( $n=0$  to 29: positive/ LTP pulses,  $n=30$  to 59: LTD pulse units). (b) Non-linearity of the LTP curve is quantified as  $\alpha_P$  and that of the LTD curve as  $\alpha_D$ . After curve-fitting using the method provided in the text, we obtain  $\alpha_P = 3.875$ ,  $\alpha_D = -3.84$ . Asymmetry=  $|\alpha_P - \alpha_D| = 7.715$  (c)  $R_{xy}$  vs pulse number ( $n$ ) when the pulse sequence in (a) is repeated over 10 cycles. . . . . 55

4.1 (a) Schematic of the ferromagnetic free layer for the device without defects, red colour corresponds to magnetic moments pointing vertically down ( $m_z = -1$ ) and blue colour corresponds to moments pointing up ( $m_z=1$ ) (b) Schematic of the ferromagnetic free layer for the device with defects, which are essentially triangular regions with modified PMA (more details in the text) . . . . . 60

4.2 (a) **Device without defects:** For positive weight update/ long-term potentiation or LTP (red plot), positive pulses of current density  $1 \times 10^7$  A/cm<sup>2</sup> have been applied in the presence of a 3000 G in-plane magnetic field. For negative weight update/ long-term depression or LTD (black plot), 20 negative pulses of current density  $1 \times 10^7$  A/cm<sup>2</sup> have been applied under the same 3000 G field. Both for LTP and LTD, each such programming current pulse is of 1 ns pulse width. We have allowed 100 ns delay between any two consecutive pulses. **Device with defects:** For positive weight update/ long-term potentiation or LTP (pink plot), positive pulses of current density  $3 \times 10^7$  A/cm<sup>2</sup> have been applied in the presence of a 3000 G in-plane magnetic field. For negative weight update/ long-term depression or LTD (brown plot), 20 negative pulses of current density  $3 \times 10^7$  A/cm<sup>2</sup> have been applied under the same 3000 G field. Same pulse width and delay between pulses are used as in (a). **For both devices,** average out-of-plane (OOP) magnetization ( $m_z$ ) at the end of the delay is plotted as a function of pulse number. Thus,  $m_z$  here includes domain-wall motion both during the pulse and during the delay. (b) For non-linearity and asymmetry quantification of the device without defects,  $m_z$  in (a) is first converted to conductance (through TMR effect) and then normalized (minimum conductance =0, maximum conductance =1 ). Then, by fitting curves based on the equations provided with the NeuroSim simulator [108, 118, 123], the following numbers are obtained. **Device without defects:** non-linearity factor of LTP  $\alpha_p = 2.47$  (red plot), non-linearity factor of LTD  $\alpha_d = - 2.45$  (black plot) , and asymmetry=  $|\alpha_p - \alpha_D| = 4.92$ . **Device with defects:** LTP (pink plot) and LTD (brown plot) curves are extremely linear, so the synaptic characteristic can be considered ideal with  $\alpha_p = \alpha_d = 0$ , and hence asymmetry also 0. . . . . 62

4.3 **Device without defects:** (a) Magnetization configuration images ‘just after’ programming pulse  $n$  is applied for LTP and ‘before’ the next pulse ( $n + 1$ ) pulse is applied for LTP (the time gap between the two is the delay time between pulses: 100 ns). Here,  $n = 2, 3, 10, 11$ . The cyan colour represents vertical up magnetic moments i.e.,  $m_z = 1$ , and red represents vertically down state  $m_z = - 1$ . (b) Magnetization configuration images ‘just after’ programming pulse  $n$  is applied for LTD and ‘before’ the next pulse ( $n + 1$ ) pulse is applied for LTD (the time gap between the two is the delay time: 100 ns). Here,  $n = 22, 23, 30, 31$ . (More details are provided in the text.) . . . . . 63

4.4	<b>Device with defects:</b> (a) Magnetization configuration images ‘just after’ programming pulse $n$ is applied for LTP and ‘before’ the next pulse $(n + 1)$ pulse is applied for LTP. Here, $n = 2, 3, 10, 11$ . The cyan colour represents vertical up magnetic moments i.e., $m_z = 1$ , and red represents vertically down state $m_z = -1$ . (b) Magnetization configuration images ‘just after’ programming pulse $n$ is applied for LTD and ‘before’ the next pulse $(n + 1)$ pulse is applied for LTD. Here, $n = 22, 23, 30, 31$ . (More details are provided in the text.) . . . . .	64
4.5	Domain wall (DW) velocity vs current density for the device without defects (black plot) and the one with defects (red plot) . . . . .	67
4.6	(a) For a device without defects, after initiating the domain wall at one end of the device, like in Fig. 4.3, average out-of-plane (OOP) magnetization ( $m_z$ ) of the ferromagnetic layer increases steadily in the absence of programming pulses, suggesting that the domain wall moves towards the center to minimize the energy due to dipole interaction between moments. This is true at different temperature values. (b) The same simulation as in (a) is carried out for the device with defects. This time $m_z$ changes very little in the beginning but then attains a steady value. This is true across a wide range of temperature values (0 K to 300 K). (c) Standard deviation/ fluctuation in $m_z$ , proportional to the domain-wall motion, is plotted as a function of temperature for the device without defects and the one with defects. . . . .	68
4.7	Domain wall (DW) velocity vs. current density for different gap lengths between consecutive defects. . . . .	72
5.1	(a) Schematic showing occurrence of spin current ( $J_s$ ) in a stack with a single layer of ferromagnetic metal (shown with light green colour here) and a single layer of heavy metal (shown with orange colour). (b) Schematic showing occurrence of spin current ( $J_s$ ) in a stack with multiple repetitions of heavy metal (HM) (orange) -ferromagnetic metal (FM) (green) bi-layers, with the thickness of the heavy metal increasing from bottom to top. In the stack of (a), an extra oxide layer is needed to promote PMA, which is not the case with the multi-layer stack of (b). . . . .	77

5.2 (a) Gradient heavy-metal-and-ferromagnet multi-layer stack, in which the thickness of the heavy metal (Pt) increases from bottom to top layer in increments of 0.4 nm, while the thickness of each ferromagnetic layer (Co) is fixed. (b) XRR spectra of our gradient Pt/Co multi-layer stack; black circle corresponds to the measured data, and the red solid line is fitted data. From fitting, we have extracted the thickness of every layer of our gradient-Pt/Co multilayer, which is shown in (c). The Pt layer's thickness is increased from bottom to top, as confirmed by this XRR-based thickness analysis. (d) XRD spectra of the same multi-layer thin stack. (e) SQUID magnetometry: Normalized out-of-plane magnetization vs out-of-plane magnetic field ( $H_z$ ). (f) Normalized in-plane magnetization vs in-plane magnetic field ( $H_x$ ). The anisotropy field (corresponding to PMA):  $H_k = 1.2$  T or 12 kG. . . . . 81

5.3 (a) Schematic of SOT-switching measurements on the device: both read and write current pulses are applied along  $x$  axis, Hall voltage is measured in the  $y$ -direction ( $V_y$ ), and constant in-plane assisting field along  $x$  axis. (b) Read current is applied in the  $x$ -direction ( $I_x$ ), and Hall voltage ( $V_y$ ) is measured along  $y$  direction, with magnetic field swept in  $z$  direction. Anomalous Hall resistance ( $R_{xy}$ ), which is the ratio of  $V_y$  to  $I_x$  and is proportional to the out-of-plane magnetization component ( $M_z$ ), is plotted as a function of out-of-plane magnetic field ( $H_z$ ). (c) and (d) Anomalous Hall resistance ( $R_{xy}$ ) vs applied current density (write pulse) for different pulse widths at  $H_x = -500$  G (c) and 500 G (d) (out-of-plane field  $H_z = 0$  throughout). (e) Critical current density for switching vs  $\ln(t_{\text{pulse}}/\tau_0)$  for  $H_x = -500$  G (out-of-plane field  $H_z = 0$  throughout). Black plot: positive current pulses, Red plot: negative current pulses. Thermal stability factor ( $\Delta$ ) is calculated to be 65 from this measurement, as explained in text. (f) MOKE images corresponding to intermediate states between saturated up and down states as current pulses of different magnitudes are applied under a fixed in-plane magnetic field ( $H_x = -500$  G and 500 G) and zero out-of-plane field ( $H_z = 0$ ). All these measurements are carried out at room temperature of device D1. . . . . 83

5.4	SOT switching and thermal stability of device D2: (a) and (b) Anomalous Hall resistance $R_{xy}$ vs current density plots for in-plane field $H_x = -500$ G and $+500$ G respectively. The out-of-plane field $H_z$ is zero throughout. The duration of each SOT-generating pulse ( $t_{pulse}$ ) is 1 ms for (a) and (b). (c) The critical current density for switching vs $\ln(t_{pulse}/\tau_0)$ for $H_x = -500$ G. Here $t_{pulse}$ varies from 100 $\mu$ s to 5 ms. From the linear fitting of this plot using Eq. 1 of the main manuscript, we have determined the thermal stability factor to be 62 for device D2. . . . .	86
5.5	SOT switching and thermal stability of device D3: (a) and (b) Anomalous Hall resistance $R_{xy}$ vs current density plots for in-plane field $-500$ G and $+500$ G respectively. The out-of-plane field $H_z$ is zero throughout. The duration of each SOT-generating pulse is 1 ms for (a) and (b). (c) The critical current density for switching vs $\ln(t_{pulse}/\tau_0)$ for $H_x = -500$ G. Here, $t_{pulse}$ ranges from 100 $\mu$ s to 10 ms, and obtained thermal stability from (c) for device D3 is 65. . . . .	86
5.6	SOT switching and thermal stability of device D4: (a) and (b) Anomalous Hall resistance $R_{xy}$ vs. current density plots for $H_x = -500$ G and $+500$ G, respectively, using 1 ms pulse-width SOT pulses. (c) The critical current density for switching vs $\ln(t_{pulse}/\tau_0)$ for $H_x = -500$ G, where $t_{pulse}$ ranges from 60 $\mu$ s to 10 ms. Thermal stability factor obtained thereby from (c) for device D4 is 64. . . . .	87
5.7	Summary of the thermal stability and critical current density measured for the four devices. . . . .	87
5.8	(a) Schematic of Harmonics Hall measurements: AC current applied in the x-direction and harmonics voltage measured in y-direction (b) First and second harmonic resistance vs longitudinal magnetic field ( $H_x$ ) for current density = $6.8 \times 10^6$ A/cm <sup>2</sup> (c) Second harmonic resistance ( $R_{2\omega}$ ) vs longitudinal magnetic field ( $H_x$ ) for different densities ranging from 0.67 to $10.3 \times 10^6$ A/cm <sup>2</sup> . (d) $H_{DL}$ as a function of current density and from linear fitting we obtained $\chi_{SOT} = H_{DL}/J = -4.80 \times 10^{-6}$ Oe cm <sup>2</sup> /A. . . . .	88

5.9 (a) LTP and LTD plots of the gradient-Pt/Co-multi-layer device: 30 identical positive pulses of current density  $3.03 \times 10^7$  A/cm<sup>2</sup> are applied for LTP ( $R_{xy}$  increases with pulse number), and 30 identical negative pulses of current density  $-3.24 \times 10^7$  A/cm<sup>2</sup> are applied for LTD ( $R_{xy}$  decreases with pulse number) under in-plane magnetic field:  $H_x = 500$  G (out-of-plane field  $H_z = 0$  G). (b) Difference between  $R_{xy}$  of two consecutive states ( $\Delta R_{xy}$ ) plotted as a function of pulse number. (c), (d): the stability/ retention of 30 consecutive LTP states and 24 consecutive LTD state (from (a)) over time. (e) Standard deviation of  $R_{xy}$  over time, obtained from (c), (d) for each LTP/ LTD state, plotted as a function of pulse number ( $n$ ) to obtain each state. (f)  $R_{xy}$  from (a) is normalized between 0 and 1 and plotted against normalized pulse number, and values of non-linearity coefficients  $\alpha_P$  and  $\alpha_D$  are extracted. (g) Average and standard deviation (error bar) of  $R_{xy}$  for each LTP and each LTD state over 20 full LTP-LTD cycles. All these measurements are carried out at room temperature. . . . . 90

6.1 **Switching mechanism due to SOT and crystal structure Mn<sub>3</sub>Sn.** (a) A schematic for the switching of the perpendicular magnetization using conventional SOT; a charge current is injected in the x-direction, which generates the spin current in the z-direction via SHE, having y-spin polarization. Due to spin-current, damping-like torque ( $M \times (M \times y)$ ) is exerted on the magnetization. To obtain the SOT switching, an in-plane assisting magnetic field is required in the case of conventional SOT. (b) A schematic for the switching utilizing the unconventional SOT: a charge current injected in the x-direction, which generates a spin current having out-of-plane spin polarization (z-spin polarization). This spin current exerts an out-of-plane damping-like torque, which is given ( $M \times (M \times z)$ ), which helps in field-free switching. . . . . 98

6.2 (a) The crystal structure of non-collinear antiferromagnet Mn<sub>3</sub>Sn having *c*-plane orientation.(b) Material stack for Mn<sub>3</sub>Sn-based sample, Mn<sub>3</sub>Sn acts as a spin current source, and Pt(1.25 nm)/Co(1.2 nm)/Pt(1.25 nm) multilayer for PMA; (c) X-ray diffraction spectra of the Ru(5 nm)/Mn<sub>3</sub>Sn (25 nm)/Pt(1 nm) thin film deposited on *c*-plane sapphire, which confirm the *c*-plane growth of the Mn<sub>3</sub>Sn and (d) X-ray reflectivity (XRR) spectra of the thin film; measured XRR data (wine circle) with simulated data (dark yellow line). . . . . 101

6.3	(a) Polar MOKE measurements: normalized MOKE intensity vs. the out-of-plane magnetic field for reference (black solid line with circle) and Mn <sub>3</sub> Sn-based (red solid line with circle) samples. (b) Normalized out-of-plane magnetization ( $M_z/M_s$ ) vs. out-of-plane magnetic field ( $H_z$ ) for reference and Mn <sub>3</sub> Sn-based samples. (c) Normalized in-plane magnetization ( $M_x/M_s$ ) vs. in-plane magnetic field ( $H_z$ ) for reference and Mn <sub>3</sub> Sn samples. (b) and (c) confirm the presence of PMA in both the samples, reference and Mn <sub>3</sub> Sn-based samples having an anisotropy field. $H_K = 0.75$ T. . . . .	102
6.4	(a) Material stack with Mn <sub>3</sub> Sn (b) SEM image of the Hall bar in which current applied at 120 w.r.t. $[1\bar{1}00]$ direction and magnetization states were determined using MOKE microscopy (c) MOKE images for different current densities, confirms the magnetization switching from +z to -z state for $H_x = +500$ G. (d) Magnetization switching from -z to +z state for $H_x = -500$ G. All measurements performed using pulsed current of pulsed width = 50 $\mu$ s and at room temperature. . . . .	103
6.5	(a) SEM image of the Hall bar device (b) MOKE images of field-free switching measurements: as current density increases, the switching % also increases. During these measurements, $H_z = 0$ and $H_x = 0$ , pulse width=200 $\mu$ s. . . . .	104
6.6	MOKE images of the reference sample initially saturated in +z state. (a) and (b) MOKE images for the different current densities in the presence of the assisting magnetic field +500 G and -500 G, respectively. In these measurements, a 500 $\mu$ s pulse width is utilized for the pulsed current at room temperature. The reference sample does not exhibit any SOT switching. . . . .	105
6.7	MOKE images of the reference sample initially saturated in -z state. (a) and (b) MOKE images for assisting field +500 G and -500 G, respectively. A 500 $\mu$ s pulse width is used for the pulsed current at room temperature in these studies. There is no SOT switching in the reference sample, which is consistent with the Fig. 6.6. . . . .	105
6.8	Temperature dependence coercivity and exchange bias of the Mn <sub>3</sub> Sn-based sample. . . . .	106

# List of Tables

3.1	Summary of the optimization parameters, power, and growth rate. . . . .	48
3.2	Comparison of the spintronics devices performance with RRAM for synaptic behavior [124, 127]. . . . .	58
4.1	Table showing how duration of LTP/ LTD pulse and energy dissipated per LTP/ LTD pulse scale with length of the device (which is in turn proportional to the distance between two consecutive defects), while the synaptic weight resolution of the device has been kept fixed at 4 bits. . . . .	72
5.1	Recently reported experimentally obtained switching current density and thermal stability factor ( $\Delta$ ) values for different devices consisting of a single layer of heavy metal (Pt or Pt-Cu or Pt-Cr alloy) and a single layer of ferromagnetic metal (Co), as compared to the values reported here for the gradient Pt/Co multi-layer device. . . . .	85
6.1	Summary of the thickness and surface/interface roughness of the Ru/Mn <sub>3</sub> Sn/Pt/Co/Pt heterostructures extracted from the XRR fitting. . . . .	102